QM/MM Simulations of the Covalent Inhibition of the SARS-CoV-2 Main Protease: Four Compounds and Three Reaction Mechanisms

Bella L. Grigorenko[a], Igor Polyakov[a], Goran Giudetti[b], Shirin Faraji[c], Anna I. Krylov[b,*], and Alexander V. Nemukhin[a]

[a] *Department of Chemistry, Lomonosov Moscow State University, Moscow, 119991, Russia*

[b] *Department of Chemistry, University of Southern California, Los Angeles, California, 90089-0482, United States*

[c] *Zernike Institute for Advanced Materials, University of Groningen, Groningen, 9747 AG, The Netherlands and*

* *Corresponding author: krylov@usc.edu*

The search for efficient inhibitors of the SARS-CoV-2 enzymes remains important due to the continuing COVID-19 pandemic. We report the results of computational modeling of the reactions of the SARS-CoV-2 main protease (M^{Pro}) with four potential covalent inhibitors. Two of them, carmofur and nirmatrelvir, have been shown experimentally the ability to inhibit M^{Pro}. Two other compounds, X77A and X77C, were designed computationally in this work, derived from the structure of X77, a non-covalent inhibitor forming a tight surface complex with M^{Pro}. We modified the X77 structure by introducing warheads capable of efficient chemical reactions with the catalytic cysteine residue in the M^{Pro} active site. The reactions of the four molecules with M^{Pro} were investigated by quantum mechanics/molecular mechanics (QM/MM) calculations. According to calculations, the reactions for all four compounds are exothermic, with sufficiently low barriers, suggesting efficient inhibition of the enzyme. From the chemical perspective, the four compounds react with M^{Pro} following three distinct mechanisms. In all cases, the reaction is initiated by a nucleophilic attack of the thiolate group of the deprotonated cysteine residue from the catalytic dyad Cys145-His41 of M^{Pro}. In the case of carmofur and X77A, the covalent binding of the thiolate to the ligand involves the formation of the fluoro-uracil leaving group. The reaction with X77C follows the nucleophilic aromatic substitu-

tion S_NAr mechanism. The reaction of M^{Pro} with nirmatrelvir, which has a reactive nitrile group, leads to the formation of the covalent thioimidate adduct with the thiolate of the Cys145 residue in the enzyme active site.

TOC graphics:

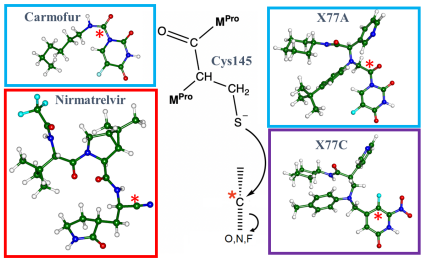

I. INTRODUCTION

The quantum mechanics/molecular mechanics (QM/MM) methods are indispensable tools for modeling biochemical reactions in complex environments[1–14]. QM/MM affords calculations of energy profiles of enzyme-catalyzed reactions as well as reactions of the covalent inhibition of enzymes. The latter are of particular interest due to the COVID-19 threats, which stimulated massive efforts, including computer simulations, aiming to reveal molecular-level mechanisms of the action of SARS-CoV-2 enzymes and to design efficient non-covalent and covalent inhibitors to inactivate troublesome enzymes[1].

The present work contributes to this effort by modeling reactions of four compounds with the critical SARS-CoV-2 enzyme, the main protease (M^{Pro}), also known as the 3 chymotrypsin-like protease ($3CL^{Pro}$)[15,16]. This enzyme, encoded by the viral genome, plays an important role in cleaving viral polyproteins into functional proteins. Thus, inhibiting this enzyme would block viral replication[15–22], making M^{Pro} an attractive drug target.

QM/MM-based computer simulations provide insights into reaction mechanisms and can be used to predict novel compounds as prospective drugs[23–35]. Numerous studies investigated irreversible (or covalent) inhibitors of cysteine proteases, to which M^{Pro} belongs[17,36–45]. The list of prospective inhibitors is constantly growing; however, mechanisms of their interaction with the enzyme are not yet fully elucidated. In this work, we consider two compounds, carmofur[22,46,47] and nirmatrelvir[48,49], which have already been identified as the irreversible

inhibitors of M^{Pro}. We also introduce two novel compounds, called X77A and X77C. We designed these molecules computationally, starting from the structure of X77, a potent non-covalent inhibitor[50,51] of M^{Pro}. X77 is capable of forming a tight surface complex with SARS-CoV-2 M^{Pro}, whose structure has been deposited in the Protein Data Bank[52] (PDB ID: 6W63).

Fig. 1 shows structures of the compounds considered in this work. As we discuss below, the reactions of all four compounds with the catalytic amino acid residue Cys145 of M^{Pro} involve the nucleophilic attack of the Cys145 thiolate on the target carbon atom of the inhibitor (red asterisks in Fig. 1 mark these target carbon atoms), however, the detailed mechanisms are different. Carmofur, 1-hexylcarbamoyl-5-fluorouracil, shown in the upper left panel in Fig. 1, is a known drug for the treatment of colorectal cancer[47]. Nirmatrelvir, (1R,2S,5S)-N-[(1S)-1-cyano-2-[(3S)-2-oxopyrrolidin-3-yl]ethyl]-3-[(2S)-3,3-dimethyl-2-[(2,2,2-trifluoroacetyl)amino]butanoyl]-6,6-dimethyl-3-azabicyclo[3.1.0]hexane-2-carboxamide, shown in the lower left panel in Fig. 1, is also known as the substance PF-07321332 developed by Pfizer. This compound is an active component of the approved oral drug Paxlovid for the treatment of COVID-19[48].

The two new molecules designed in this work were derived computationally from the structure of X77, N-(4-tert-butylphenyl)-N-[(1R)-2-(cyclohexylamine)-2-oxo-1-(pyridin-3-yl)ethyl]-1H-imidazole-4-carboxamid, which several studies[50,51] described as a promising non-covalent inhibitor of M^{Pro}. According to the results of molecular docking[51], the binding energy of X77 to M^{Pro} is very high (ΔG $\sim$-10 kcal/mol), giving rise to the dissociation constant of 0.057 μM. Several mimetic studies[50] used X77 as the basis for deriving novel non-covalent inhibitors of M^{Pro}. We follow a different strategy, aiming to develop effective covalent inhibitors. Specifically, we propose to modify X77 by introducing warhead groups capable of efficient chemical reactions with the catalytic cysteine residue in the M^{Pro} active site (see the right panels in Fig. 1). In other words, we propose to turn an efficient non-covalent inhibitor into a covalent inhibitor.

So far, only two computational papers[35,53]investigated the interaction of carmofur and nirmatrelvir with M^{Pro}. Our recent study[53] was devoted mainly to the methodological aspects of QM/MM simulations of enzyme-catalyzed reactions and used the carmofur-M^{Pro} system as an example. Ramos-Guzmán *et al.* have reported estimates of free-energy profiles of the reactions of the covalent inhibition of M^{Pro} by several molecules, including nirmatrelvir,

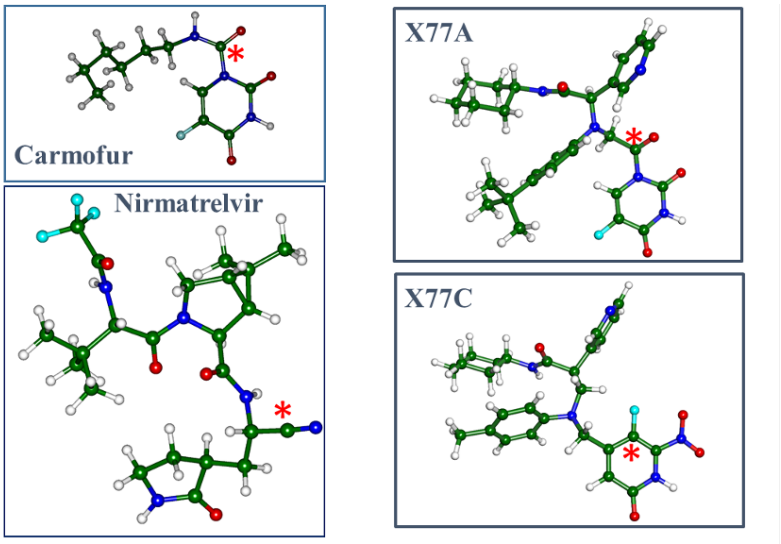

FIG. 1: Molecular models of the compounds considered in this work as covalent inhibitors of M^{Pro}. Here and in all figures, carbon atoms are colored green, oxygen—red, nitrogen—blue, sulfur—yellow, fluorine—cyan, hydrogen—white. Red asterisks mark the target carbon atoms of the nucleophilic attack of the Cys145 thiolate of M^{Pro}.

carried out using a common computational approach[32–35].

According to the current knowledge, as illustrated in the left part in Fig. 2, reactions of the covalent binding of the catalytic Cys145 of M^{Pro} is initiated by the proton transfer from cysteine to its partner in the catalytic dyad, His41, followed by the nucleophile attack of the sulfur ion on the target carbon atom of the ligand[17,23–45,54–58] (e.g., see discussion in Ref. 41). The emerging negative charge on the atom X adjacent to the target carbon atom is modulated by the oxyanion hole formed by the chain Asn142-Gly143-Ser144-Cys145. In the present work, X is either oxygen, or nitrogen, or fluorine. The right panel in Fig. 2 shows the anticipated configuration of the reaction product.

Therefore, the following structural elements are important for modeling the inhibition reaction: the side chains in the catalytic dyad (Cys145/His41) and the oxyanion hole (Asn142-Gly143-Ser144-Cys145); this is common for all four compounds considered in this work. The differences are as follows. In reactions with carmofur, X77A, and X77C, the formation of the covalent bond between the sulfur and carbon atoms is accompanied by the leaving group (fluoro-uracil for carmofur and X77A, fluorine ion for X77C), whereas in the reaction with nirmatrelvir, there is a proton rearrangement, which saturates the emerging valency in the

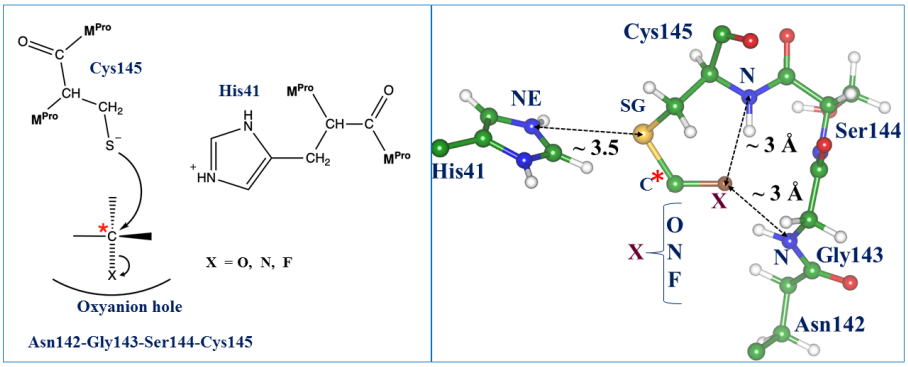

FIG. 2: Left: Scheme of the inhibition reaction; red asterisks mark the target carbon atoms of the nucleophilic attack of the Cys145 thiolate. Right: Representative structure of the product showing the oxyanion hole motif. Distances between the sulfur atom SG in Cys145 and the nitrogen NE atom in His41, and the distances between nitrogen atoms in the anion hole and the atom X (X is O, or N, or F in this study) are given in Å.

nitrile nitrogen. Mechanisms of the creation of the leaving groups may also follow different scenarios. These important details of the reaction mechanisms are the focus of our study.

II. SYSTEM PREPARATION AND QM/MM DETAILS

Several crystal structures of M^{Pro} and its complexes with various ligands are available in the Protein Data Bank (PDB)[52]. Fig. 3 shows the fragments of the active site of M^{Pro}, as they appear in the PDB structures. We focus on the aspects relevant to the chemical reactions of the selected compounds (Fig. 1) with Cys145. As mentioned above, we pay attention to the position of the catalytic dyad side chains, Cys145 and His41, as well as of the oxyanion hole chain Asn142-Gly143-Ser144-Cys145.

We used the crystal structure (PDB ID: 7BUY[22]) of M^{Pro} with the aliphatic tail of the carmofur molecule attached to Cys145 as a template for building model systems for simulating the M^{Pro}–carmofur reaction. Because we started modeling the M^{Pro}–nirmatrelvir reaction before knowing relevant crystal structures of the reaction products, we used the template of the M^{Pro}–carmofur model system to construct the M^{Pro}–nirmatrelvir model.

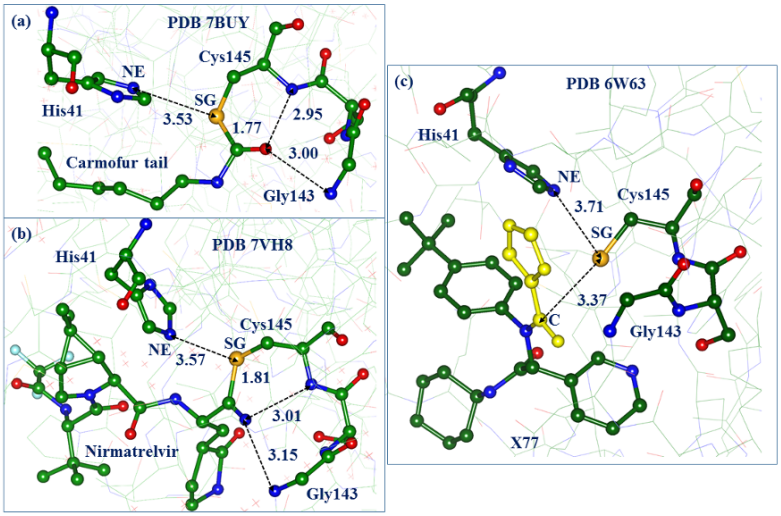

FIG. 3: Fragments of the M^{Pro} active site from selected PDB structures. Panels (a) and (b): fragments of the active site of M^{Pro} relevant to the reactions of selected compounds with Cis145 as they appear in the PDB structures. We focus on the chain Asn142-Gly143-Ser144-Cys145 with the reactive Cys145 and the oxyanion hole groups and to the His41 side chain location relative to Cys145. Panel (c): the PDB structure 6W63, a non-covalent complex of M^{Pro} with X77. The molecular group of X77 (highlighted in yellow) is replaced by reactive warheads to design covalent inhibitors (see panels X77A and X77C in Fig. 1).

After we completed simulations, we used the crystal structure (PDB ID: 7VH8)[22] to verify the predictions of our QM/MM modeling.

We used the crystal structure (PDB ID: 6W63, the right panel in Fig. 3) of the complex of the non-covalent inhibitor X77 with M^{Pro} to construct molecular models for the reactions with the compounds X77A and X77C. Importantly, our docking calculations show that these modified structures (X77A and X77C, see Fig. 1) have binding energies similar to the parent X77: -8.9 kcal/mol for X77A and -9.4 kcal/mol for X77C, to be compared with -9.74 kcal/mol (our computed value for X77) or the literature value of -10.2 kcal/mol[51]. Therefore, the proposed molecules X77A and X77C exhibit a high affinity with the catalytic site of the enzyme. The corresponding molecular models of the protein with the X77A and X77C molecules were prepared manually using molecular mechanics tools.

The partitioning of the model systems into the QM and MM parts for each compound is explained in Section III and in the Supporting Information (SI). As we illustrated in our QM/MM study of the M^{Pro}–carmofur model[53], reporting only relevant structures from

PDB as initial coordinates of heavy atoms and the partitioning of the system into QM and MM parts is not sufficient to ensure the reproducibility of QM/MM calculations of energies of enzymatic reactions. More details need to be reported for others to be able to assess the implications of the results and to reproduce the findings. In the SI we provide details of the preparation of the model systems, including addition of hydrogen atoms and the protonation states of the amino acid side chains, solvation of proteins, initial relaxation of structures using classical molecular dynamics, link-atom schemes in the QM/MM boundary treatment, embedding protocols, and optimization algorithms. In the main manuscript we focus on the chemical aspects of these reactions.

We use the following notations for the computed stationary points on the potential energy surfaces (PES): REAC (reactant state), IP (ion-pair state), PROD (product state), INT (intermediate), TS (transition state). For each system, the REAC structure refers to the neutral state Cys145/His41 in the catalytic dyad; IP corresponds to the structure with the ion-pair state Cys^{-}/His^{+}, PROD corresponds to the structure with the covalently bound Cys145 and with a leaving group kept in the active site. Possible reaction intermediates INT and transition states TS are numbered sequentially for each reaction.

The QM/MM optimized coordinates of the REAC, IP, INT, PROD structures were obtained in series of unconstrained minimization. TS structures were optimized in series of constrained minimization, assuming proper reaction coordinates. The features of TSs, separating the corresponding minimum energy points, were verified by performing forward and backward descent from the located saddle points. Further details are presented in Section III and in the SI. The calculations at the QM(PBE0-D3/6-31G*)/MM(AMBER) level were carried out with the NWChem[59] and Q-Chem[60,61] software packages.

The optimized coordinates of all structures are deposited to the COVID-19 hub repository supported by MolSSI (see the SI for a complete list of deposited files).

III. RESULTS AND DISCUSSION

A. Reaction of M^{Pro} with carmofur

Fig. 4 shows the computed energy profile for the reaction of M^{Pro} with carmofur. The reaction occurs in two steps: REAC→TS1→IP and IP→TS2→PROD. In our previous study[53],

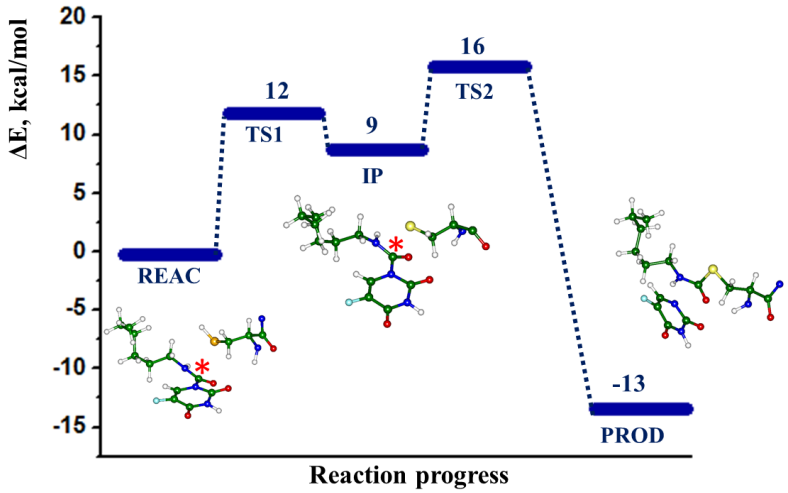

FIG. 4: The computed energy profile for the M^{Pro} - carmofur reaction. The insets show the essential features of the REAC, IP and PROD states.

we characterized only the second step using QM/MM approach with a slightly different QM-MM partitioning. Here we consider the entire reaction including the step of the ion-pair ($Cys145^{-}$/$His41^{+}$) formation. In the present calculations, the QM subsystem consisted of 155 atoms, including carmofur, His41 and Cys145 sidechains, the detailed description is given in the SI. In order to account for conformational flexibility of the enzyme-substrate complex and verify the Fig. 4 results for the REAC→TS1→IP stage we conducted an additional QM/MM molecular dynamics simulation. The obtained results confirm Fig. 4 and are described in the SI.

Selection of reaction coordinates for this reaction is trivial. At the step of IP formation REAC→TS1→IP, two-dimensional energy plot along the distances from the transferring proton to the SG atom of Cys145 and NE atom of His41 allowed us to estimate the TS1 point and to obtain the REAC and IP structures. At the next step IP→TS2→PROD, the distance between SG and the carbonyl carbon atom (C7) in the carmofur molecule served as a reaction coordinate.

In this case, we can use the only available piece of experimental information, the crystal structure of the reaction product, to validate our simulations. Fig. 5 shows the active site of the computed product structure (colored balls and sticks) and compares it with the relevant fragment (yellow sticks) of the crystal structure (PDB ID: 7BUY[22]). We observe a good agreement for the key distances between the two structures (see also Fig. 3). The distance

between heavy atoms SG and NE in the catalytic dyad, as well as the selected distances in the oxyanion hole region between the nitrogen atoms of the protein and the oxygen atom (O7) in the adduct of the protein with the carmofur tail are consistent between the calculations and the crystal structure, taking into account that the leaving group (the fluoro-uracil warhead) is not present in the crystal structure but kept in the active site of the model system.

As in our previous QM/MM calculations for this system[53], we conclude that the simulations correctly describe the reaction and that the results are consistent with the experimental observation that carmofur binds covalently to M^{Pro} and can act as an efficient inhibitor. The estimated barrier height of 16 kcal/mol and the reaction energy -13 kcal/mol are within the target range for effective covalent inhibitors.

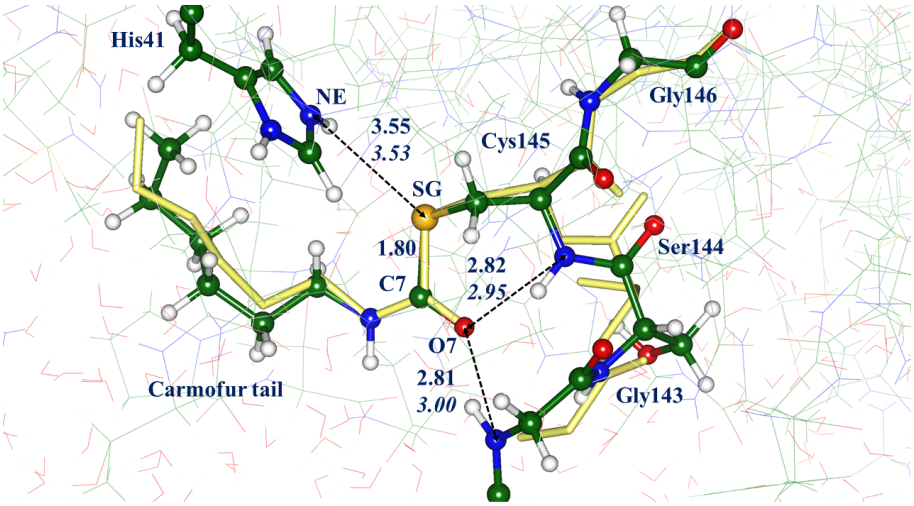

FIG. 5: Structure of the product in the reaction with carmofur. The fragment in yellow sticks refers to the crystal structure 7BUY (cf. Fig. 3) superimposed on the computed structure. The distances are in Å; the values in italics correspond to the crystal structure.

B. Reaction of M^{Pro} with nirmatrelvir

The molecular model of nirmatrelvir is shown in the lower left panel in Fig. 1. Its interaction with the surface of M^{Pro} studied by classical molecular dynamics simulations[49] shows a tight binding of this compound to the protein. The covalent binding of nirmatrelvir by M^{Pro} is established experimentally—it is clearly seen in the reported crystal structures (PDB IDs 7VH8[48], 7MLG, 7MLF). The reaction of M^{Pro} with a nitrile-based ligand, such

as nirmatrelvir, should lead to a covalent thioimidate adduct after deprotonation of Cys145 (i.e. formation of the $Cys145^{-}/His41^{+}$ ion pair) and the nucleophilic attack of the thiolate leading to the S-C covalent bond.[35,44]

According to our results, there are two elementary steps of the reaction: (i) formation of the ion-pair state through a direct proton transfer from Cys145 to His41 (without a mediating water molecule as was assumed in Ref. 35) and (ii) formation of the covalently bound adduct. The second step is coupled with the proton transfer over the hydrogen-bond wire comprising several molecular groups in the active site, as explained below. We constructed the model system by using the carmofur model as a template. The QM subsystem consisted of 257 atoms, including the nirmatrelvir molecule, His41, Gly143, Ser144, Cys145 and water molecules (see the SI for details).

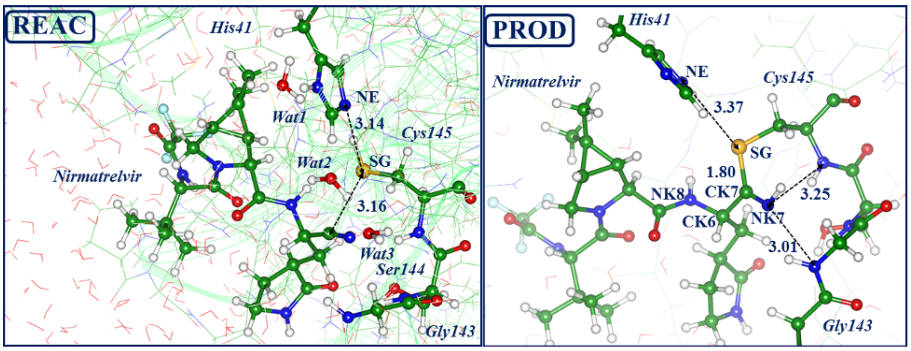

FIG. 6: Reactants (REAC) and products (PROD) structures in the reaction of M^{Pro} with nirmatrelvir.

The left panel of Fig. 6 shows the REAC structure. We show the reacting species, nirmatrelvir, the catalytic dyad Cys145-His41, the chain of the residues forming the oxyanion hole, Gly143-Ser144-Gys145, and three water molecules (denoted as Wat1, Wat2, Wat3) that constitute the proton wire. Note that the nirmatrelvir molecule is located in the solvent-accessible region, practically on the surface separating the protein (shown schematically by light green ribbons) and the solvating water shell (shown by red-white lines). The key distances from the sulfur atom in Cys145 to the NE atom of His41 and to the target carbon atom CK7 of the nirmatrelvir molecule are 3.14 and 3.16 Å, respectively.

The right panel of Fig. 6 shows the PROD structure. One can clearly see the covalent adduct captured in the active site, with the SG-CK7 bond length of 1.80 Å and the N-N distances in the oxyanion hole, 3.25 and 3.01 Å, in good agreement with the respective

distances from the crystal structure, 3.01 and 3.15 Å (see Fig. 3). The computed torsion angle NK8-CK6-CK7-NK7 (153°) practically coincides with that in the crystal (150°).

Fig. 7 presents the computed energy profile, which shows that the formation of the ion pair step is characterized by small energy changes: E(TS1) $\sim$ 3 kcal/mol, E(IP) $\sim$ 2 kcal/mol; geometry changes are also small relative to REAC.

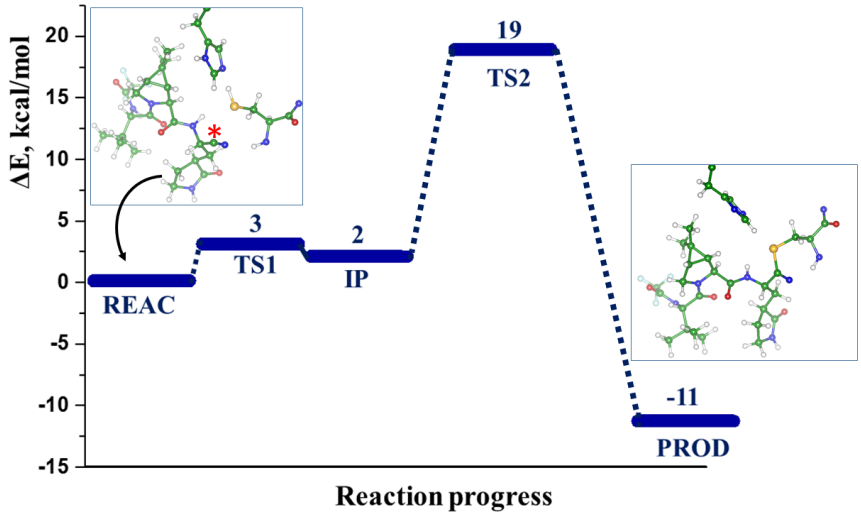

FIG. 7: The computed energy profile for the M^{Pro}–nirmatrelvir reaction. The insets show the essential features of REAC and PROD.

Let us now discuss the mechanism of the formation of the covalent thioimidate adduct. There is no obvious path for proton transfer from either from NE or ND atoms of His41 to the nitrile nitrogen NK7; the corresponding distances NE-NK7 and ND-NK7 are 5.3 and 6.2 Å. We carefully analyzed possible proton wires, which could connect nitrogen atoms of His41 and the nitrile nitrogen atom NK7. We found no suitable pathways with only one mediating water molecule as assumed in Ref.[35], but identified a more complicated pathway comprising several groups. Fig. 8 shows the structure in the vicinity of the barrier separating the ion-pair and product states. The proton wire, marked by magenta arrows, extends over the His41-Wat1-Thr25-Wat2-Wat3-Nirmatrelvir chain. Fig. 8 shows the distances between protons and the nearest heavy atoms. The inset, which depicts the products, shows, in particular, distances between heavy atoms along the proton wire, which are typical for this hydrogen-bonded construct.

It is difficult to locate precisely the corresponding transition state by using QM/MM calculations due to an extremely labile proton wire. Therefore, in Fig. 7 we give only an

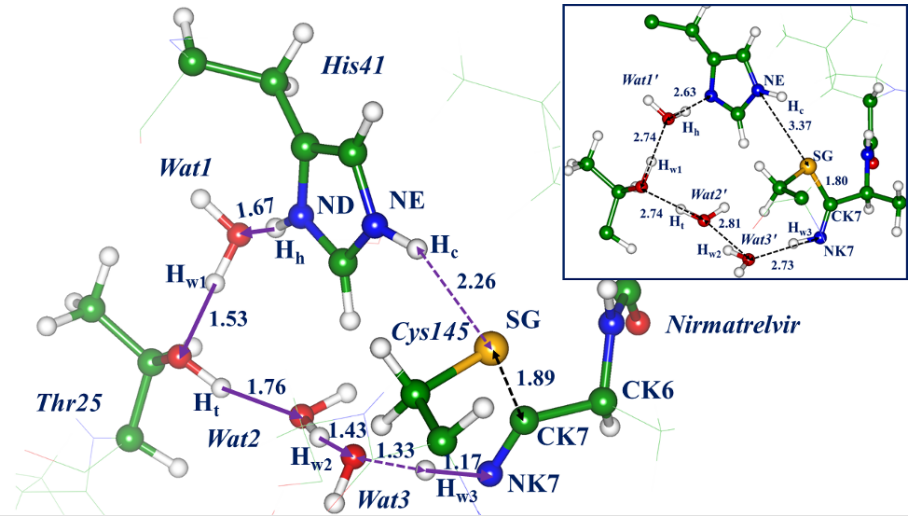

FIG. 8: Structure of transition state between the ion-pair and the product states. The inset shows the product state in another perspective than in Fig. 6.

estimate from above of the energy barrier at the second reaction step. We note that the estimates of the energy differences between structures along the reaction pathway, REAC-IP-TS2-PROD (0, 2, 19, -11 kcal/mol) are consistent with the estimates along the free energy profile computed in Ref. 35 (0, 2, 16.3, -9.5 kcal/mol).

C. Reaction of M^{Pro} with X77A

The X77A compound (shown in the upper right part in Fig. 1) was designed computationally by introducing the warhead with the fluoro-uracil moiety resembling that in the carmofur molecule (the upper left part in Fig. 1). The target atom for the nucleophile attack of the Cys145 thiolate is the similar carbonyl carbon atom marked by the asterisk. Thus, it is reasonable to expect that the mechanism of the reaction M^{Pro} with X77A might resemble that in the reaction with carmofur with the same leaving group. Indeed, the basic features are common, but the computed energy profile shown in Fig. 9 is more complicated with an additional reaction intermediate INT2 besides the ion-pair intermediate IP.

The first step REAC→TS1→IP is practically the same as in the carmofur reaction, but with slightly lower barrier (8 kcal/mol for X77A as compared to 12 kcal/mol for carmofur). As shown in Fig. 9, the pathway from IP first leads to the intermediate INT2 with a considerably lower energy (-12 kcal/mol) then the level of REAC. The step IP→TS2→INT2

corresponds to a large conformational change in the X77A molecule in the enzyme active site, whereas the distance of the nucleophile attack (the SG-C distance), remains almost the same at this step. The INT2 conformation favors the formation of the SG-C covalent bond at the step INT2→TS3→PROD, which occurs with a low barrier of 4 kcal/mol. The product structure PROD lies 23 kcal/mol below the level of reactants REAC. Therefore, according to our simulations, the X77A compound should be a more efficient inhibitor of M^{Pro} that carmofur—the reaction barriers are lower and the reaction energy is higher.

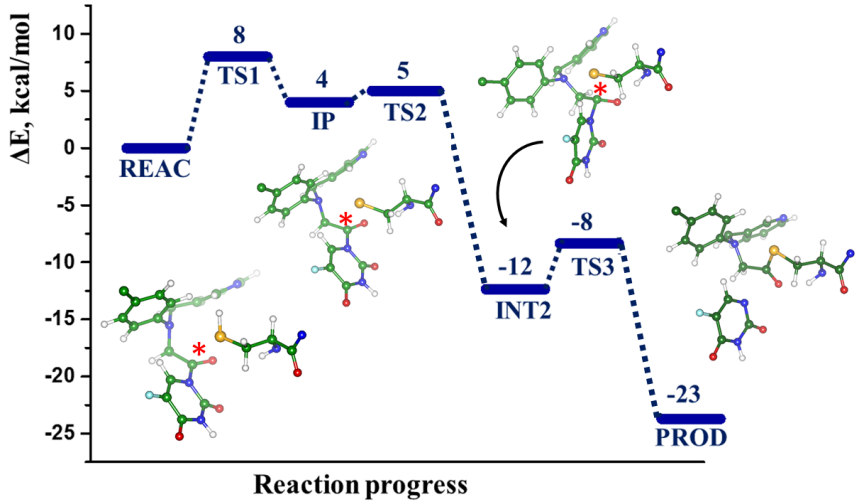

FIG. 9: The computed energy profile for the M^{Pro}-X77A reaction. The insets show the essential features of the REAC, IP, INT2 and PROD states.

D. Reaction of M^{Pro} with X77C

Klein *et al.* proposed[45] to use aromatic compounds that can react with the catalytic cysteine by the S_NAr addition/elimination mechanism as a new class of covalent inhibitors of cysteine proteases. Several such compounds have been tested as prospective inhibitors of the protease rhodesain[45]. Inspired by this idea, we introduced the 5-fluoro-6-nitro-pyrimidine-2,4(1H,3H)-dione warhead into the X77 template to create compound X77C (see Fig. 1). Upon deprotonation, the sulfur ion of Cys145 attacks the carbon atom C5 initially bound to fluorine.

Fig. 10 shows the computed reaction pathway and Fig. 11 illustrates the structures corresponding to the computed minimum energy points along the pathway from REAC

to PROD via two reaction intermediates—the ion-pair state and the Meisenheimer complex, designated as INT2. Although the reaction follows the known patterns of the S_NAr transformations[45,62,63], the nature of the Meisenheimer complex in each reaction is still debated, in particular, whether it represents a reaction intermediate or a transition state. In our simulations, the Meisenheimer complex appears as a well defined local minimum (INT2) on the PES between the transition states TS2 and TS3.

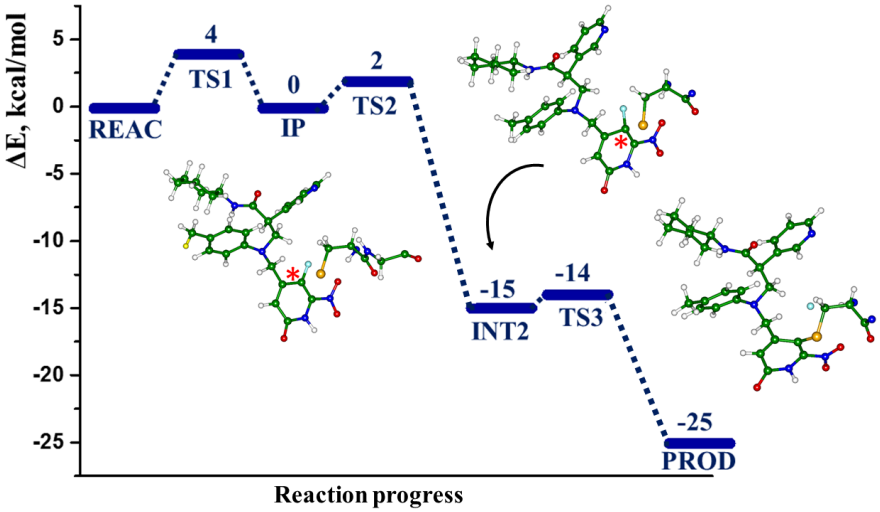

FIG. 10: The computed energy profile for the M^{Pro} - X77C interaction. The inset show the essential features of the IP, INT2 and PROD states.

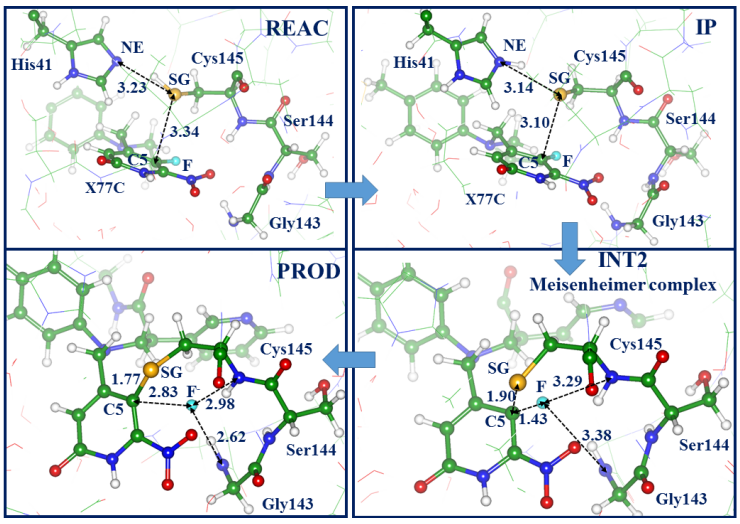

FIG. 11: Structures along the pathway in the reaction of M^{Pro} with X77C.

IV. DISCUSSION

The COVID-19 pandemic motivated numerous studies of the SARS-related enzymes, which considerably expanded the understanding of the enzyme catalysis. Our study contributes to these efforts. We modeled reactions of four compounds and show that these compounds are capable to bind chemically to the catalytic cysteine residue of M^{Pro} and, therefore, to serve as irreversible inhibitors of this enzyme. The simulations revealed three distinct reaction mechanisms. We recognize that these three mechanisms do not exhaust all possible scenarios—other documented examples of the M^{Pro} inhibition include the Michael addition to the unsaturated carbon-carbon bond[31,32] and the reactions with ketones[30,34].

The design of potential drugs cannot be accomplished on the basis of QM/MM calculations alone. Yet, the simulations contribute to the ongoing efforts to find more effective drugs to fight COVID-19. We show that the employed computational protocols are sufficiently reliable and produce the results consistent with the already known information: the computed energy profiles for carmofur and nirmatrelvir show that the corresponding reactions with M^{Pro} are efficient with respect to energy barriers and reaction energies. Therefore, we expect that the compounds designed computationally in our work, X77A and X77C, and characterized at the same level of theory are also promising drug candidates. We note that the energy profiles for their reactions with M^{Pro} show lower energy barriers and higher reaction energies. Although calculations of free-energy reaction profiles provide a more complete description of protein-ligand interaction than QM/MM simulations of stationary PES points, accurate estimates of the relative energies of the key structures along the reaction coordinate are sufficient to characterize prospective covalent inhibitors. Of course, for non-covalent inhibitors, free-energy calculations are more important. We note that free-energy calculations present more challenges in terms of the reproducibility of the results than the PES calculations[53], as vividly illustrated by the calculations of free energy surface for the N3-M^{Pro} interaction[31,32].

In this work we employed a QM/MM approach with PBE0 functional in the QM part to describe large model systems with 150–250 atoms in the QM region. If the goal of the QM/MM-based calculations is the drug design, then much lower level could be applied, for example semi-empirical approaches (e.g., AM1, DFTB). We stress that according to Ref. 53, reliability and reproducibility problems in QM/MM appear even at a high level of theoretical treatment. As documented[53], the barrier heights on PES can only be estimated

within error bars of up to 5 kcal/mol due to the inherent problems of QM/MM protocols. On the positive note, this slightly simplifies simulations, because the precise location of saddle points (transition states), which requires expensive calculations of the Hessian matrices can be avoided. If the search of covalent inhibition is concerned, it is sufficient to ensure that such barriers, computed in series of constrained minimization, are smaller than the values typical for efficient enzymes, say, 14-17 kcal/mol. This is the case for the calculations and predictions described in this work.

V. CONCLUSIONS

The results of our QM/MM modeling of chemical reactions of the catalytic Cys145 amino acid residue of the SARS-CoV-2 main protease with four compounds, carmofur, nirmatrelvir, X77A, X77C, show that these species can form stable covalent adducts with M^{Pro}, and the activation barriers are sufficiently low for the reactions to be effective. The results for carmofur and nirmatrelvir are consistent with the experimental findings, and the success of the simulations provides a sound basis for a prediction of the two novel potential inhibitors, X77A and X77C, proposed in this work. From the fundamental perspective, this study illustrates that the formation of covalent adducts follow three distinct reaction mechanisms of the irreversible inhibition of cysteine proteases.

VI. ACKNOWLEDGMENT

While finalizing this manuscript, one of the authors (AIK) contracted COVID-19 and was treated by the currently available drug Paxlovid, which contains nirmatrelvir (PF-07321332) as an active ingredient targeting M^{pro}.

We thank Dr. S.V. Lushchekina for help with the molecular docking calculations. This work was supported by the U.S. National Science Foundation (No. CHE-1856342 to AIK) and by the Russian Science Foundation (grant No. 19-73-20032 to IVP, BLG and AVN). We used the Extreme Science and Engineering Discovery Environment (XSEDE), which is supported by National Science Foundation grant number ACI-1548562 (XSEDE resource: Comet; allocation ID: TG-CHE200131). We also acknowledge resources of MolSSI. IVP,

BLG, and AVN also acknowledge the use of HPC computing resources at the Lomonosov Moscow State University.

The authors declare the following competing financial interest(s): A.I.K. is the president and a part-owner of Q-Chem, Inc.

---

[1] K. Gao, R. Wang, J. Chen, L. Cheng, J. Frishcosy, Y. Huzumi, Y. Qiu, T. Schluckbier, X. Wei, and G. Wei, Methodology-centered review of molecular modeling, simulation, and prediction of SARS-CoV-2, Chem. Rev. **122**, 11287 (2022).

[2] A. Warshel and M. Levitt, Theoretical studies of enzymatic reactions: Dielectric electrostatic and steric stabilization of the carbonium ion in the reaction of lysozyme, J. Mol. Biol. **103**, 227 (1976).

[3] H. M. Senn and W. Thiel, QM/MM methods for biomolecular systems, Angew. Chem., Int. Ed. **48**, 1198 (2009).

[4] M. Liu, Y. Wang, Y. Chen, M. J. Field, and J. Gao, QM/MM through the 1990s: The first twenty years of method development and applications, Isr. J. of Chem. **54**, 1250 (2014).

[5] M. W. van der Kamp and A. J. Mulholland, Combined quantum mechanics/molecular mechanics (QM/MM) methods in computational enzymology, Biochemistry **52**, 2708 (2013).

[6] K. Świderek, I. Tuñón, and V. Moliner, Predicting enzymatic reactivity: from theory to design, WIREs: Comput. Mol. Sci. **4**, 407 (2014).

[7] L. Hu, P. Söderhjelm, and U. Ryde, Accurate reaction energies in proteins obtained by combining QM/MM and large QM calculations, J. Chem. Theory Comput. **9**, 640 (2013).

[8] A. Monari, J. L. Rivail, and X. Assfeld, Theoretical modeling of large molecular systems. Advances in the local self consistent field method for mixed quantum mechanics/molecular mechanics calculations, Acc. Chem. Res. **46**, 596 (2013).

[9] E. Brunk and U. Rothlisberger, Mixed quantum mechanical/molecular mechanical molecular dynamics simulations of biological systems in ground and electronically excited states, Chem. Rev. **115**, 6217 (2015).

[10] H. J. Kulik, J. Zhang, J. P. Klinman, and T. J. Martínez, How large should the QM region be in QM/MM calculations? The case of catechol o-methyltransferase, J. Phys. Chem. B **120**,

11381 (2016).

[11] S. F. Sousa, A. J. M. Ribeiro, R. P. P. Neves, N. F. Brás, N. M. F. S. A. Cerqueira, P. A. Fernandes, and M. J. Ramos, Application of quantum mechanics/molecular mechanics methods in the study of enzymatic reaction mechanisms, WIREs: Comput. Mol. Sci. **7**, e1281 (2017).

[12] Q. Cui, T. Pal, and L. Xie, Biomolecular QM/MM simulations: What are some of the "burning issues"?, J. Phys. Chem. B **125**, 689 (2021).

[13] F. Lipparini and B. Mennucci, Hybrid QM/classical models: Methodological advances and new applications, Comp. Phys. Rep. **2**, 041303 (2021).

[14] C. E. Tzeliou, M. A. Mermigki, and D. Tzeli, Review on the QM/MM methodologies and their application to metalloproteins, Molecules **27** (2022).

[15] K. Anand, J. Ziebuhr, P. Wadhwani, J. R. Mesters, and R. Hilgenfeld, Coronavirus main proteinase (3CLpro) structure: basis for design of anti-SARS drugs, Science **300**, 1763 (2003).

[16] Z. Jin, X. Du, Y. Xu, Y. Deng, M. Liu, Y. Zhao, B. Zhang, X. Li, L. Zhang, C. Peng, Y. Duan, J. Yu, L. Wang, K. Yang, F. Liu, R. Jiang, X. Yang, T. You, X. Liu, X. Yang, . Bai, H. Liu, X. Liu, L. W. Guddat, W. Xu, G. Xiao, C. Qin, Z. Shi, H. Jiang, Z. Rao, and H. Yang, Structure of Mpro from SARS-CoV-2 and discovery of its inhibitors, Nature **582** (2020).

[17] L. Zhang, D. Lin, X. Sun, U. Curth, C. Drosten, L. Sauerhering, S. Becker, K. Rox, and R. Hilgenfeld, Crystal structure of SARS-CoV-2 main protease provides a basis for design of improved α-ketoamide inhibitors, Science **368**, 409 (2020).

[18] R. Cannalire, C. Cerchia, A. R. Beccari, F. S. Di Leva, and V. Summa, Targeting SARS-CoV-2 proteases and polymerase for covid-19 treatment: State of the art and future opportunities, J. of Med. Chem. **65**, 2716 (2022).

[19] S. Ullrich, V. M. Sasi, M. C. Mahawaththa, K. B. Ekanayake, R. Morewood, J. George, L. Shuttleworth, X. Zhang, C. Whitefield, G. Otting, C. Jackson, and C. Nitsche, Challenges of short substrate analogues as SARS-CoV-2 main protease inhibitors, Bioorg. & Med. Chem. Lett. **50**, 128333 (2021).

[20] Q. Li and C. Kang, Progress in developing inhibitors of SARS-CoV-2 3C-like protease, Microorganisms **8** (2020).

[21] W. Dai, B. Zhang, X. Jiang, H. Su, J. Li, Y. Zhao, X. Xie, Z. Jinand J. Peng, F. Liu, C. Li, Y. Li, F. Bai, H. Wang, X. Cheng, X. Cen, S. Hu, X. Yang, J. Wang, X. Liu, G. Xiao, H. Jiang, Z. Rao, L. Zhang, Y. Xu, H. Yang, and H. Liu, Structure-based design of antiviral drug

candidates targeting the SARS-CoV-2 main protease, Science **368**, 1331 (2020).

[22] Z. Jin, Y. Zhao, Y. Sun, B. Zhang, H. Wang, Y. Wu, Y. Zhu, C. Zhu, T. Hu, X. Du, Y. Duan, J. Yu, X. Yang, X. Yang, K. Yang, X. Liu, L. W. Guddat, G. Xiao, L. Zhang, H. Yang, and Z. Rao, Structural basis for the inhibition of SARS-CoV-2 main protease by antineoplastic drug carmofur, Nat. Struct. & Mol. Bio. **27**, 529 (2020).

[23] S. Ma, L. S. Devi-Kesavan, and J. Gao, Molecular dynamics simulations of the catalytic pathway of a cysteine protease: a combined QM/MM study of human cathepsin k, J. Am. Chem. Soc. **129**, 13633 (2007).

[24] A. G. Taranto, P. Carvalho, and M. A. Avery, QM/QM studies for michael reaction in coronavirus main protease (3CL pro), J. Mol. Graph. Model. **27**, 275 (2008).

[25] G. Oanca, M. Asadi, A. Saha, B. Ramachandran, and A. Warshel, Exploring the catalytic reaction of cysteine proteases, J. Phys. Chem. B **124**, 11349 (2020).

[26] D. Wei, X. Huang, J. Liu, M. Tang, and C. Zhan, Reaction pathway and free energy profile for papain-catalyzed hydrolysis of N-Acetyl-Phe-Gly 4-Nitroanilide, Biochemistry **52**, 5145 (2013).

[27] K. Świderek and V. Moliner, Revealing the molecular mechanisms of proteolysis of SARS-CoV-2 Mpro by QM/MM computational methods, Chem. Sci. **11**, 10626 (2020).

[28] C. A. Ramos-Guzmán, J. J. Ruiz-Pernía, I., and Tuñón, Unraveling the SARS-CoV-2 main protease mechanism using multiscale methods, ACS Cat. **10**, 12544 (2020).

[29] M. G. Khrenova, V. G. Tsirelson, and A. V. Nemukhin, Dynamical properties of enzyme–substrate complexes disclose substrate specificity of the SARS-CoV-2 main protease as characterized by the electron density descriptors, Phys. Chem. Chem. Phys. **22**, 19069 (2020).

[30] D. Mondal and A. Warshel, Exploring the mechanism of covalent inhibition: Simulating the binding free energy of α-ketoamide inhibitors of the main protease of SARS-CoV-2, Biochemistry **48**, 4601 (2020).

[31] K. Arafet, N. Serrano-Aparicio, A. Lodola, A. J. Mulholland, F. V. González, K. Swiderek, and V. Moliner, Mechanism of inhibition of SARS-CoV-2 Mpro by N3 peptidyl michael acceptor explained by QM/MM simulations and design of new derivatives with tunable chemical reactivity, Chem. Sci. **12**, 1433 (2021).

[32] C. A. Ramos-Guzmán, J. J. Ruiz-Pernía, I., and Tuñón, A microscopic description of SARS-CoV-2 main protease inhibition with Michael acceptors. Strategies for improving inhibitor design, Chem. Sci. **12**, 3489 (2021).

[33] C. A. Ramos-Guzmán, J. J. Ruiz-Pernía, and Tuñón, Multiscale simulations of SARS-CoV-2 3CL protease inhibition with aldehyde derivatives. Role of protein and inhibitor conformational changes in the reaction mechanism, ACS Cat. **11**, 4157 (2021).

[34] C. A. Ramos-Guzmán, J. J. Ruiz-Pernía, and Tuñón, Inhibition mechanism of SARS-CoV-2 main protease with ketone-based inhibitors unveiled by multiscale simulations: Insights for improved designs, Angew. Chem., Int. Ed. **60**, 25933 (2021).

[35] C. A. Ramos-Guzmán, J. J. Ruiz-Pernía, and Tuñón, Computational simulations on the binding and reactivity of a nitrile inhibitor of the SARS-CoV-2 main protease, Chem. Comm. **57**, 9096 (2021).

[36] H.-H. Otto and T. Schirmeister, Cysteine proteases and their inhibitors, Chem. Rev. **97**, 133 (1997).

[37] J. C. Powers, J. L. Asgian, Ö. D. Ekici, and K. E. James, Irreversible inhibitors of serine, cysteine, and threonine proteases, Chem. Rev. **102**, 4639 (2002).

[38] K. Arafet, S. Ferrer, and V. Moliner, First quantum mechanics/molecular mechanics studies of the inhibition mechanism of cruzain by peptidyl halomethyl ketones, Biochemistry **54**, 3381 (2015).

[39] K. Arafet, S. Ferrer, and V. Moliner, Computational study of the catalytic mechanism of the cruzain cysteine protease, ACS Cat. **7**, 1207 (2017).

[40] K. Arafet, S. Ferrer, F. V. González, and V. Moliner, Quantum mechanics/molecular mechanics studies of the mechanism of cysteine protease inhibition by peptidyl-2,3-epoxyketones, Phys. Chem. Chem. Phys. **19**, 12740 (2017).

[41] K. Arafet, K. Świderek, and V. Moliner, Computational study of the michaelis complex formation and the effect on the reaction mechanism of cruzain cysteine protease, ACS Omega **3**, 18613 (2018).

[42] J. R. A. Silva, L. Cianni, D. Araujo, P. H. J. Batista, D. Vita, F. Rosini, A. Leitao, J. Lameira, and C. A. Montanari, Assessment of the cruzain cysteine protease reversible and irreversible covalent inhibition mechanism, J. Chem. Inf. Mod. **60**, 880 (2020).

[43] A. M. Dos Santos, L. Cianni, D. De Vita, F. Rosini, A. Leitão, C. A. Laughton, J. Lameira, and C. A. Montanari, Experimental study and computational modelling of cruzain cysteine protease inhibition by dipeptidyl nitriles, Phys. Chem. Chem. Phys. **20**, 24317 (2018).

[44] C. H. S. da Costa, V. Bonatto, A. M. Dos Santos, J. Lameira, A. Leitaob, and C. A. Montanari,

Evaluating QM/MM free energy surfaces for ranking cysteine protease covalent inhibitors, J. Chem. Inf. Mod. **60**, 880 (2020).

[45] P. Klein, P. Johe, A. Wagner, S. Jung, J. Kühlborn, F. Barthels, S. Tenzer, U. Distler, W. Waigel, B. Engels, U. A. Hellmich, T. Opatz, and T. Schirmeister, New cysteine protease inhibitors: Electrophilic (het)arenes and unexpected prodrug identification for the trypanosoma protease rhodesain, Molecules **25**, 1451 (2020).

[46] W. Vuong, M. B. Khan, C. Fischer, E. Arutyunova, T. Lamer, J. Shields, H. A. Saffran, R. T. McKay, M. J. van Belkum, M. A. Joyce, H. S. Young, D. L. Tyrrell, J. C. Vederas, and M. J. Lemieux, Feline coronavirus drug inhibits the main protease of SARS-CoV-2 and blocks virus replication, Nat. Comm. **11**, 4282 (2020).

[47] J. Sakamoto, C. Hamada, M. Rahman, S. Kodaira, K. Ito, H. Nakazato, Y. Ohashi, and M. Yasutomi, An individual patient data meta-analysis of adjuvant therapy with carmofur in patients with curatively resected colon cancer, Jap. J. of Clin. Onc. **35**, 536 (2005).

[48] D. R. Owen, C. M. N. Allerton, A. S. Anderson, L. Aschenbrenner, M. A, S. Berritt, B. Boras, R. D. Cardin, A. Carlo, K. J. Coffman, A. Dantonio, L. Di, H. Eng, R. Ferre, K. S. Gajiwala, S. A. Gibson, S. E. Greasley, B. L. Hurst, E. P. Kadar, A. S. Kalgutkar, J. C. Lee, J. Lee, W. Liu, S. W. Mason, S. Noell, J. J. Novak, R. S. Obach, K. Ogilvie, N. C. Patel, M. Pettersson, D. K. Rai, M. R. Reese, M. F. Sammons, J. G. Sathish, R. S. P. Singh, C. M. Steppan, A. E. Stewart, J. B. Tuttle, L. Updyke, P. R. Verhoest, L. Wei, Q. Yang, and Y. Zhu, An oral SARS-CoV-2 Mpro inhibitor clinical candidate for the treatment of COVID-19, Science **374**, 1586 (2021).

[49] B. Ahmad, M. Batool, Q. U. Ain, M. S. Kim, and S. Choi, Exploring the binding mechanism of PF-07321332 SARS-CoV-2 protease inhibitor through molecular dynamics and binding free energy simulations, Int. J. Mol. Sci. **22** (2021).

[50] A. M. Andrianov, Y. V. Kornoushenko, A. D. Karpenko, I. P. Bosko, and A. V. Tuzikov, Computational discovery of small drug-like compounds as potential inhibitors of SARS-CoV-2 main protease, J. Biomol. Struct. and Dyn. **39**, 5779 (2021).

[51] V. V. Welborn, Beyond structural analysis of molecular enzyme-inhibitor interactions, El. Struct. **4**, 014006 (2022).

[52] H. M. Berman, J. Westbrook, Z. Feng, G. Gilliland, T. N. Bhat, H. Weissig, I. N. Shindyalov, and P. E. Bourne, The protein data bank, Nucleic Acids Research **28**, 235 (2000).

[53] G. Giudetti, I. Polyakov, B. L. Grigorenko, S. Faraji, A. V. Nemukhin, and A. I. Krylov, How

reproducible are QM/MM simulations? Lessons from computational studies of the covalent inhibition of the SARS-CoV-2 main protease by carmofur, J. Chem. Theory Comput. (2022), in press; https://doi.org/10.1021/acs.jctc.2c00286.

[54] F. Richter, R. Blomberg, S. D. Khare, G. Kiss, A. P. Kuzin, A. J. T. Smith, J. Gallaher, Z. Pianowski, R. C. Helgeson, A. Grjasnow, R. Xiao, J. Seetharaman, Min Su, S. Vorobiev, S. Lew, F. Forouhar, G. J. Kornhaber, J. F. Hunt, G. T. Montelione, L. Tong, K. N. Houk, D. Hilvert, and D. Baker, Computational design of catalytic dyads and oxyanion holes for ester hydrolysis, J. Am. Chem. Soc. **134**, 16197 (2012).

[55] A. Paasche, T. Schirmeister, and B. Engels, Benchmark study for the cysteine–histidine proton transfer reaction in a protein environment: Gas phase, COSMO, QM/MM approaches, J. Chem. Theory Comput. **9**, 1765 (2013).

[56] A. Paasche, A. Zipper, S. Schäfer, J. Ziebuhr, T. Schirmeister, and B. Engels, Evidence for substrate binding-induced zwitterion formation in the catalytic Cys-His dyad of the SARS-CoV main protease, Biochemistry **53**, 5930 (2014).

[57] M. Chen and C. Chen, Rational design of high-performance phosphine sulfonate nickel catalysts for ethylene polymerization and copolymerization with polar monomers, ACS Cat. **7**, 1308 (2017).

[58] L. Zanetti-Polzi, M. D. Smith, C. Chipot, J. C. Gumbart, D. L. Lynch, A. Pavlova, J. C. Smith, and I. Daidone, Tuning proton transfer thermodynamics in SARS-CoV-2 main protease: Implications for catalysis and inhibitor design, J. Phys. Chem. Lett. **12**, 4195 (2021).

[59] E. Aprá, E. J. Bylaska, W. A. de Jong, N. Govind, K. Kowalski, T. P. Straatsma, M. Valiev, H. J. J. van Dam, Y. Alexeev, J. Anchell, V. Anisimov, F. W. Aquino, R. Atta-Fynn, J. Autschbach, N. P. Bauman, J. C. Becca, D. E. Bernholdt, K. Bhaskaran-Nair, S. Bogatko, P. Borowski, J. Boschen, J. Brabec, A. Bruner, E. Cauët, Y. Chen, G. N. Chuev, C. J. Cramer, J. Daily, M. J. O. Deegan, T. H. Dunning, M. Dupuis, K. G. Dyall, G. I. Fann, S. A. Fischer, A. Fonari, H. Früchtl, L. Gagliardi, J. Garza, N. Gawande, S. Ghosh, K. Glaesemann, A. W. Götz, J. Hammond, V. Helms, E. D. Hermes, K. Hirao, S. Hirata, M. Jacquelin, L. Jensen, B. G. Johnson, H. Jónsson, R. A. Kendall, M. Klemm, R. Kobayashi, V. Konkov, S. Krishnamoorthy, M. Krishnan, Z. Lin, R. D. Lins, R. J. Littlefield, A. J. Logsdail, K. Lopata, W. Ma, A. V. Marenich, J. M. del Campo, D. Mejia-Rodriguez, J. E. Moore, J. M. Mullin, T. Nakajima, D. R. Nascimento, J. A. Nichols, P. J. Nichols, J. Nieplocha, A. Otero de-la Roza,

B. Palmer, A. Panyala, T. Pirojsirikul, B. Peng, R. Peverati, J. Pittner, L. Pollack, R. M. Richard, P. Sadayappan, G. C. Schatz, W. A. Shelton, D. W. Silverstein, D. M. A. Smith, T. A. Soares, D. Song, M. Swart, H. L. Taylor, G. S. Thomas, V. Tipparaju, D. G. Truhlar, K. Tsemekhman, T. Van Voorhis, Á. Vázquez-Mayagoitia, P. Verma, O. Villa, A. Vishnu, K. D. Vogiatzis, D. Wang, J. H. Weare, M. J. Williamson, T. L. Windus, K. Woliński, A. T. Wong, Q. Wu, C. Yang, Q. Yu, M. Zacharias, Z. Zhang, Y. Zhao, and R. J. Harrison, NWChem: Past, present, and future, J. Chem. Phys. **152**, 184102 (2020).

[60] A. I. Krylov and P. M. W. Gill, Q-Chem: An engine for innovation, WIREs: Comput. Mol. Sci. **3**, 317 (2013).

[61] E. Epifanovsky, T. B. Gilbert, X. Feng, J. Lee, Y. Mao, N. Mardirossian, P. Pokhilko, A. F. White, M. P. Coons, A. L. Dempwolff, Z. Gan, D. Hait, P. R. Horn, L. D. Jacobson, I. Kaliman, J. Kussmann, A. W. Lange, K. U. Lao, D. S. Levine, J. Liu, S. C. McKenzie, A. F. Morrison, K. D. Nanda, F. Plasser, D. R. Rehn, M. L. Vidal, Z.-Q. You, Y. Zhu, B. Alam, B. J. Albrecht, A. Aldossary, E. Alguire, J. H. Andersen, V. Athavale, D. Barton, K. Begam, A. Behn, N. Bellonzi, Y. A. Bernard, E. J. Berquist, H. G. A. Burton, A. Carreras, K. Carter-Fenk, R. Chakraborty, A. D. Chien, K. D. Closser, V. Cofer-Shabica, S. Dasgupta, M. de Wergifosse, J. Deng, M. Diedenhofen, H. Do, S. Ehlert, P.-T. Fang, S. Fatehi, Q. Feng, T. Friedhoff, J. Gayvert, Q. Ge, G. Gidofalvi, M. Goldey, J. Gomes, C. E. González-Espinoza, S. Gulania, A. O. Gunina, M. W. D. Hanson-Heine, P. H. P. Harbach, A. Hauser, M. F. Herbst, M. Hernández Vera, M. Hodecker, Z. C. Holden, S. Houck, X. Huang, K. Hui, B. C. Huynh, M. Ivanov, A. Jász, H. Ji, H. Jiang, B. Kaduk, S. Kähler, K. Khistyaev, J. Kim, G. Kis, P. Klunzinger, Z. Koczor-Benda, J. H. Koh, D. Kosenkov, L. Koulias, T. Kowalczyk, C. M. Krauter, K. Kue, A. Kunitsa, T. Kus, I. Ladjánszki, A. Landau, K. V. Lawler, D. Lefrancois, S. Lehtola, R. R. Li, Y.-P. Li, J. Liang, M. Liebenthal, H.-H. Lin, Y.-S. Lin, F. Liu, K.-Y. Liu, M. Loipersberger, A. Luenser, A. Manjanath, P. Manohar, E. Mansoor, S. F. Manzer, S.-P. Mao, A. V. Marenich, T. Markovich, S. Mason, S. A. Maurer, P. F. McLaughlin, M. F. S. J. Menger, J.-M. Mewes, S. A. Mewes, P. Morgante, J. W. Mullinax, K. J. Oosterbaan, G. Paran, A. C. Paul, S. K. Paul, F. Pavošević, Z. Pei, S. Prager, E. I. Proynov, A. Rák, E. Ramos-Cordoba, B. Rana, A. E. Rask, A. Rettig, R. M. Richard, F. Rob, E. Rossomme, T. Scheele, M. Scheurer, M. Schneider, N. Sergueev, S. M. Sharada, W. Skomorowski, D. W. Small, C. J. Stein, Y.-C. Su, E. J. Sundstrom, Z. Tao, J. Thirman, G. J. Tornai, T. Tsuchimochi, N. M. Tubman, S. P.

Vecchan, O. Vydrov, J. Wenzel, J. Witte, A. Yamada, K. Yao, S. Yeganeh, S. R. Yost, A. Zech, I. Y. Zhang, X. Zhang, Y. Zhang, D. Zuev, A. Aspuru-Guzik, A. T. Bell, N. A. Besley, K. B. Bravaya, B. R. Brooks, D. Casanova, J.-D. Chai, S. Coriani, C. J. Cramer, G. Cserey, A. E. DePrince, R. A. DiStasio, A. Dreuw, B. D. Dunietz, T. R. Furlani, W. A. Goddard, S. Hammes-Schiffer, T. Head-Gordon, W. J. Hehre, C.-P. Hsu, T.-C. Jagau, Y. Jung, A. Klamt, J. Kong, D. S. Lambrecht, W. Liang, N. J. Mayhall, C. W. McCurdy, J. B. Neaton, C. Ochsenfeld, J. A. Parkhill, R. Peverati, V. A. Rassolov, Y. Shao, L. V. Slipchenko, T. Stauch, R. P. Steele, J. E. Subotnik, A. J. W. Thom, A. Tkatchenko, D. G. Truhlar, T. Van Voorhis, T. A. Wesolowski, K. B. Whaley, H. L. Woodcock, P. M. Zimmerman, S. Faraji, P. M. W. Gill, M. Head-Gordon, J. M. Herbert, and A. I. Krylov, Software for the frontiers of quantum chemistry: An overview of developments in the Q-Chem 5 package, J. Chem. Phys. **155**, 084801 (2021).

[62] A. J. J. Lennox, Meisenheimer complexes in S_NAr reactions: Intermediates or transition states?, Angew. Chem., Int. Ed. **57**, 2 (2018).

[63] N. A. Senger, B. Bo, Q. Cheng, J. R. Keeffe, S. Gronert, and W. Wu, The element effect revisited: Factors determining leaving group ability in activated nucleophilic aromatic substitution reactions, J. Org. Chem. **77**, 9535 (2012).